

pubs.acs.org/cm Article

# Polymorphism within the Quasi-One-Dimensional $Au_2MP_2$ (M = TI, Pb, Pb/Bi, and Bi) Series

Published as part of Chemistry of Materials special issue "C. N. R. Rao at 90."

Scott B. Lee, Jonathan S. Van Buskirk, Fatmagül Katmer, Suchismita Sarker, Daniel C. Fredrickson, and Leslie M. Schoop\*



Cite This: Chem. Mater. 2024, 36, 8217-8228



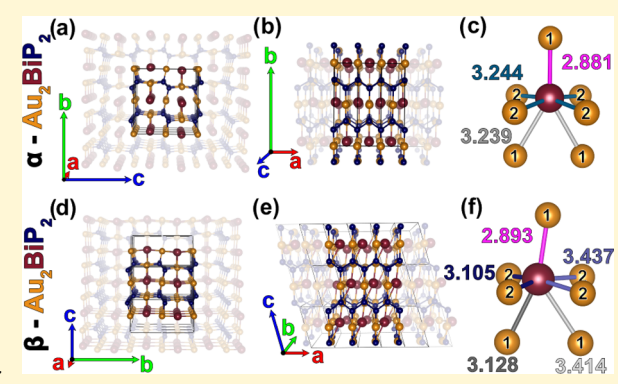
**ACCESS** 

III Metrics & More

Article Recommendations

s Supporting Information

ABSTRACT: Quasi-1-dimensional (q1D) materials have attracted significant interest for experimentally realizing fundamental physical models. A plethora of q1D systems have been discovered in previous decades, although many have not been extensively examined with modern computational or experimental techniques. Herein, we reexamine the  $Au_2MP_2$  q1D system (formerly, M = Hg, Tl, and Pb) and extend the range of M substituents to  $Pb_{0.53}Bi_{0.43}$  and Bi. Remarkably, this q1D system resists changing its highly anisotropic structure type over a range of three valence electrons per formula unit. However, at the highest valence electron count, we find that  $Au_2BiP_2$  exhibits polymorphism: in addition to the previously reported orthorhombic phase, a slight distortion generates a closely related monoclinic structure type, which is found more frequently. Analysis of



local packing tensions in the orthorhombic phase reveals strains within the  $[Au_2P_2]$  framework hold open channel spaces for the chains of M atoms, which are relatively free to move as a group within the channels. Consistent with this picture, the calculated phonon dispersions show that the monoclinic distortion in  $Au_2BiP_2$  resolves imaginary phonon frequencies seen in the orthorhombic structure type. Using density functional theory computations, we determine that this structural change is driven through rectifying both electronic and atomic packing frustrations. Furthermore, electronic transport measurements substantiate calculations of the band structures and density of states of these materials, which suggest that the compositions within this series can be tuned to band structure and property design.

### ■ INTRODUCTION

Exploration of low-dimensional materials has become a focal point for materials science due to unique electronic, 1,2 optical,<sup>3,4</sup> and thermal<sup>5,6</sup> properties that emerge in these reduced dimensions. For example, the transition metal dichalcogenides MoS2 and WS2 are stacked two-dimensional sheets that Rao's group first characterized, confined by out-oflayer van der Waals forces, where different metal coordination environments and stacking arrangements of layers directly affect catalytic efficiencies.8 Many more two-dimensional materials can be characterized by their layered structures, even if the structure does not contain a van der Waals gap, e.g., the LnSb<sub>x</sub>Te<sub>2-x- $\delta$ </sub> (Ln = lanthanide, x = 0-1,  $\delta$  = vacancy concentration) series form structures with well-defined quasitwo-dimensional layers. Here, incommensurate structural distortions, or charge density waves (CDWs), manifest within these layers arising from Fermi surface nesting in its quasi-twodimensional band structure. 10 Those CDWs have been shown to template noncollinear spin textures among Ln atoms through Ruderman-Kittel-Kasuya-Yosida interactions. 11 Now, expanding the repertoire of low-dimensional materials is important for examining how differing coordination environments, i.e., the amount of confinement, can affect physical properties.<sup>12</sup>

One interesting subset of low-dimensional materials are quasi-one-dimensional (q1D) structures—defined by having highly anisotropic motifs along one crystallographic axis, such as the recently discovered high-pressure polyhalides. Due to the confinement of electrons along one dimension, q1D materials have been reported to host unintuitive properties such as  $\Pi$ -based covalent antiferromagnetism in  $Mn_2Hg_5$ ,  $^{14-16}$  proposed spin-triplet superconductivity in  $UTe_2$  or  $K_2Cr_3As_3$ ,  $^{17,18}$  as well as q1D superconductivity in

Received: March 15, 2024 Revised: July 11, 2024 Accepted: August 16, 2024 Published: August 28, 2024





 ${
m Na}_{2-\delta}{
m Mo}_6{
m Se}_6.^1$  An ideal q1D system to examine would have a structure that contains a 1D chain of atoms that is completely decoupled from the lattice. In addition, this one-dimensional chain needs to have partially filled bands such that their bonding arrangements contribute to states near the Fermi energy. However, these requirements tend to limit options for chemical compositions, as linear chains consisting of main group elements with partially filled valence electrons obey the extended Zintl–Klemm electron counting concept only for seven electrons per chain atom (i.e., one hole in the p-manifold). Such linear geometric motifs are stabilized via hypervalent bonding, which is similar to the metavalent bonding that has been discussed by Rao.  $^{21}$ 

One intriguing exception to this electron counting scheme is the previously reported q1D  $Au_2MP_2$  (M = Hg, Tl, Pb) series. The structure, shown in Figure 1, has an

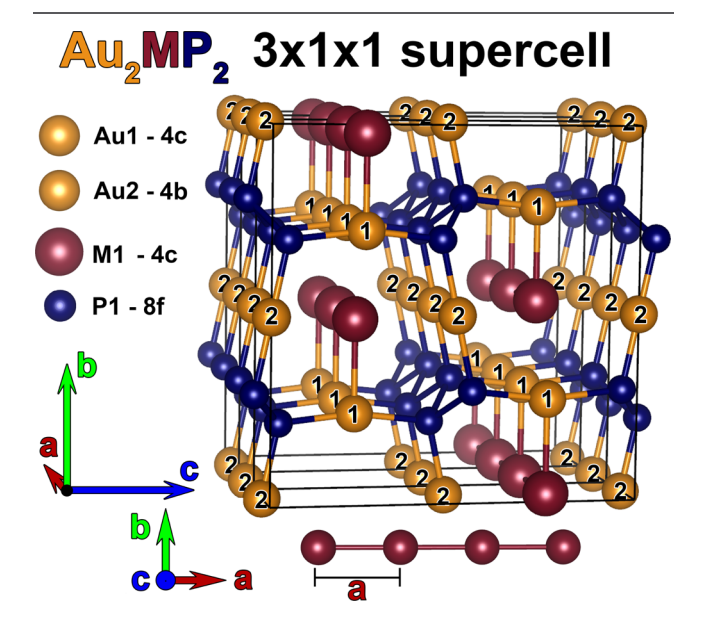


**Figure 1.** Au<sub>2</sub>MP<sub>2</sub> crystal structure, previously reported with M = Hg, Tl, and Pb. <sup>22</sup> The structure consists of a Au<sub>2</sub>P<sub>2</sub> framework, which hosts a linear chain of M guest atoms with a spacing of unit cell parameter  $a \sim 3.2$  Å.

orthorhombic unit cell with the space group Cmcm (No. 63). It consists of a covalent [Au<sub>2</sub>P<sub>2</sub>] tunnel framework filled with a linear chain of M atoms (shown in red). The large tunnel framework, comprised of a late transition metal (Au) and phosphorus, is reminiscent of the tetrel-free clathrates (e.g.,  $AM_2P_4$  (A = Sr, Ba; M = Ni, Pd, Cu),  $^{23-26}$  Ba<sub>8</sub> $M_{16}P_{30}$  (M = Au, Cu),  $^{27,28}$  Ba<sub>8</sub> $M_{24}P_{28+\delta}$  (M = Cu/Zn,  $\delta$  = 0.5–2.1),  $^{29}$  and Ba<sub>8</sub> $M_{16+y}P_{30-y}$  (M = Cu, Zn)  $^{30}$ ), which form polyhedral cages consisting of late transition metal and phosphorus atoms that surround a guest atom whose rattling (i.e., anharmonic motion) dissipates lattice thermal conductivity efficiently.<sup>31</sup> In Au<sub>2</sub>MP<sub>2</sub>, as shown in Figure 1, the metal chain (red) is relatively isolated in the tunnel with six of its seven nearestneighbors more than 3.2 Å away and only one short contact  $(\sim 2.88 \text{ Å})$  to an Au atom. The tunnel framework contains P zigzag chains (shown in blue), where P is formally in the -1oxidation state when using the 8-N rule. Every phosphorus (on the 8f Wyckoff position) is connected to two crystallographically unique Au positions. The Au 4b site (labeled as 2 in Figure 1) connects two P zigzag chains vertically along the b-axis and forms a perfectly linear geometry enforced by

symmetry and has been suggested to adopt a +1 oxidation state<sup>22,32</sup> due to similar linear coordination environments of Au in gold monohalide structures.<sup>33–35</sup> The 4c Au site (labeled as 1 in Figure 1) bridges two phosphorus atoms horizontally along the c-axis in a slightly buckled linear geometry, also justifying a 1+ charge. Thus, previous literature suggested an electron counting scheme in which the formal charge of both Au atoms is 1+, which is balanced by a zigzag chain of two [P]<sup>1-</sup> atoms. This leaves the one-dimensional chain of M atoms in a neutral oxidation state. Slight deviations from this oxidation state have been suggested due to an overlap of orbitals between the M atom and an Au1 atom ~2.88 Å away,<sup>32</sup> but computations suggested that bands of the M site dictate the electronic properties near the Fermi energy. This computational study also artificially removed the M atoms from the structure, demonstrating that the isolated "Au<sub>2</sub>P<sub>2</sub>" framework has a band gap of ~0.5 eV. With this result in conjunction with crystal orbital overlap and Hamiltonian populations showing appreciable Au-M and M-M interactions at the Fermi energy, they conclude that the expected metallicity in Au<sub>2</sub>TlP<sub>2</sub> and Au<sub>2</sub>PbP<sub>2</sub> arises from orbital mixing of the tunnel framework with the linear chain of M atoms. Still, as there is only one atom in the tunnel framework that has a short contact with the M atoms (Au1, as shown in Figure 1), it seems possible that the one-dimensional chain of atoms is relatively isolated and that 1D electronics dominate the properties of the system.

As mentioned above, the extended Zintl-Klemm concept predicts stable linear chains if each atom in the chain motif contains seven electrons. Here, the counting is most relevant for the main group elements as it refers to a filled s and an almost-filled p-shell, which has one hole. This counting scheme ignores the d-electrons. The stability of a linear chain with such electron counts stems from multicenter hypervalent bonds, i.e., interactions in which each atom has a larger number of bonding contacts than expected from their electron count, as explained by Papoian and Hoffmann. 20 Heavier elements are said to prefer such bonding over dimerization, as sp-mixing will cause the chain to dimerize. An example of a stable linear hypervalent chain with such an electron count is given by the  $Ln_5MPn_3$  (Ln = lanthanide, M = metal, Pn = pnictide) family, which can host linear Sb and Bi chains. 36,37 As we show in this work, in Au<sub>2</sub>MP<sub>2</sub>, the valence electron count can vary from 2 (only the s-shell filled) for M = Hg to 5 for M = Bi (s-shell filled and p-shell half-filled). Many of those electron counts should be unstable in a q1D motif. Especially for M = Tl, where there is nominally a single electron in the p-shell, we should expect a dimerization of the structure, similar to that shown for BiIr<sub>4</sub>Se<sub>8</sub>, where Bi forms dimerized 1D chains in a tunnel structure and formally also has an electron count of 3.19 Also, a formerly half-filled p-shell, as in the case of M = Bi, should be unstable, as half-filled bands commonly tend to distort or undergo CDW transitions.<sup>38</sup>

In fact, the first reported single-crystal X-ray characterization of  $Au_2HgP_2$  and  $Au_2TlP_2$  required multiple sites with large anisotropic thermal parameters to refine the Hg and Tl positions, further evidence toward the possibility of a modulation in the structure. Furthermore, Wen et al. computed a series of self-consistent calculations for  $Au_2PbP_2$  in which Pb positions were iteratively perturbed in 0.4 Å steps through the tunnel framework (along the chain axis), finding an energetic indifference (6.9 kcal/Pb atom) toward translation of Pb along the chain direction. This low activation

energy for ionic conductivity was theorized to be the cause of the original synthetic paper's need for multiple crystallographic M sites when refining Hg and Tl analogues.

In this paper, we reexamine the Au<sub>2</sub>MP<sub>2</sub> series with linear chain substituents M = Tl, Pb and add new members with M =  $Pb_{0.53}Bi_{0.43}$  and Bi. Phases in which M = Tl, Pb, and  $Pb_{0.53}Bi_{0.43}$ are all isotypic in the previously reported orthorhombic cell. Notably, we do not find any evidence of disorder or distortion in the M positions. Thus, the  $[Au_2P_2]$  tunnel framework is suggested to facilitate charge donated from the M atom to stabilize this variation in the valence electron count. However, when M = Bi, i.e., the highest valence electron count probed here, we find that the structure can form as a previously unreported polymorph; it does not crystallize only in the known orthorhombic cell (from here on, referred to as the  $\alpha$ phase) but also in a yet unreported, closely related, monoclinic structure type, which we will call the  $\beta$  phase. In fact, we find that  $\beta$ -Au<sub>2</sub>BiP<sub>2</sub> is formed much more frequently than the  $\alpha$ phase. Utilizing computational techniques, the stability of these two structure types is viewed through the lens of electronic minimization and relief of local packing tensions. We then connect calculated band structures with electrical transport properties, showing that compounds in this series have a tunable electronic structure, which is physically manifested as a range of compositionally dependent charge-carrier mobilities and densities. The transport properties nicely agree with expectations arising from the calculated density of states (DOS) plots. Thus, we here provide a q1D system in which the valence electron count can be tuned, allowing for targeted band structure and property design within this materials class.

## **■** EXPERIMENTAL SECTION

**Materials and Synthesis.** Safety Warning. P has a low solubility in all of the metal fluxes presented below (Tl, Pb, and Bi). Attempts to scale up this reaction may lead to an explosion of the ampules containing toxic Tl or Pb fumes. Additionally, the reacted samples occasionally contain small amounts of excess white phosphorus. Any future attempts at these syntheses and the subsequent opening of ampules should be carried out in a fumehood or properly ventilated environment.

Samples of orthorhombic Au<sub>2</sub>TlP<sub>2</sub>, Au<sub>2</sub>PbP<sub>2</sub>, Au<sub>2</sub>Pb<sub>0.53</sub>Bi<sub>0.43</sub>P<sub>2</sub>, and monoclinic  $\beta$ -Au<sub>2</sub>BiP<sub>2</sub> were synthesized using the self-flux method, utilizing a Canfield crucible. In the bottom alumina crucible, Au (Thermo Scientific, 99.999%) and red P (Alfa Aesar, 99.999+%) were loaded with the constituent metal (Tl (Thermo Scientific, 99.99%), Pb (Alfa Aesar, 99.999%), or Bi (Sigma-Aldrich, 99.999%)) in a 1:6:1 stoichiometric ratio of Au/M/P. For Au<sub>2</sub>Pb<sub>0.53</sub>Bi<sub>0.43</sub>P<sub>2</sub>, the precursors were loaded in a 1:3:3:1 ratio. The crucible was placed in a fused quartz tube and sealed under dynamic vacuum at ~70 mTorr after being backfilled three times with Ar. The sealed tube was then placed in a muffle furnace, ramped to 450 °C over 4 h, and held there for 12 h to prereact phosphorus. The furnace was then ramped to 950 °C over 5 h, kept at this temperature for 48 h, and then quickly cooled to 700 °C. At 700 °C, the cooling rate was decreased to 2 °C per hour to a target set point of 450 °C, at which point the crucible was centrifuged. All crystals were metallic gray in color.

Samples of orthorhombic  $\alpha$ -Au<sub>2</sub>BiP<sub>2</sub> were synthesized by using the same self-flux method described above but loaded in a fused-quartz tube without an alumina crucible. Quartz wool was used as the filter while centrifuging and utilized the same annealing profile as was used before. Attempts to isolate the orthorhombic phase using a Canfield crucible failed. Crystals in the orthorhombic allotrope grow in one-dimesional rods, often with an octagonal cross section, while those in the Bi monoclinic allotrope appear to lose much of their dimensionality along one axis, resulting in sheet-like rods with a rectangular cross section. Samples were not observed to fully degrade

over time in air, though crystals of the Hg analogue were reported to degrade in previous literature, <sup>22</sup> and we observed a passivating oxide layer forming in all orthorhombic systems studied here.

**Energy-Dispersive X-ray Spectroscopy.** Crystals of  $Au_2Pb_{0.53}Bi_{0.43}P_2$  that were grown in a Pb/Bi 1:1 flux crystals were characterized using energy-dispersive X-ray (EDX) spectroscopy in a Quanta environmental scanning electron microscope (SEM) equipped with an Oxford EDX detector. Compositional analysis and sample homogeneity are shown in the Supporting Information (SI).

**Powder Diffraction Experiments.** The relative phase composition of all samples was explored via powder X-ray diffraction using a STOE Stadi P powder X-ray diffractometer equipped with a Mo  $K\alpha$  ( $\lambda=0.7093\,$  Å) sealed-tube X-ray source and a graphite monochromator at room temperature in a Debye–Scherrer geometry. To do this, a representative selection of crystals was taken from each sample and ground into a fine powder along with a nondiffracting capillary to limit absorption of the heavy constituent elements. This mixture was then loaded into a 0.3 mm capillary for data collection.

**Single-Crystal Diffraction Experiments.** Small single crystals of the resulting samples were picked for single-crystal X-ray diffraction (SCXRD) analysis using an APEX2 CCD diffractometer equipped with a Mo K $\alpha$  ( $\lambda$  = 0.71073 Å) sealed-tube X-ray source and a graphite monochromator at 100 K. Indexation and integration were completed for a full hemisphere collection out to a resolution of 0.7 Å. Run list generation and frame data processing were done in APEX 2. <sup>39</sup> An analytical absorption correction was used to scale the data before importing the peak list into JANA2020. <sup>40</sup>

Chemical Pressure (CP) Analysis. Density functional theory (DFT)-chemical pressure (CP) schemes were generated for Au<sub>2</sub>MP<sub>2</sub> (M = Tl, Pb, Bi) in the orthorhombic  $(\alpha)$  phase, as well as the monoclinic  $(\beta)$  phase of Au<sub>2</sub>BiP<sub>2</sub>. DFT calculations were first performed with the ABINIT package (version 7.10.5), 41,42 employing the local density approximation (LDA) and Hartwigsen-Goedecker-Hutter norm-conserving pseudopotentials.<sup>43</sup> k-Point meshes were determined by increasing the k-point grid fineness until the total energy difference between meshes converged to less than 5 meV/ atom. The geometry of each structure was then optimized to minimize the total energy, first through the relaxation of the atomic positions with a fixed unit cell and then by releasing all geometrical parameters. It should be noted that the total energy difference for these structures is within 5 meV/atom of each other; thus, these calculations do not definitively conclude either structure as a ground state. Structural relaxations for DFT-CP were optimized with the local density approximation (LDA) exchange-correlation functionals, as is standard with DFT-CP calculations. Single point calculations were next performed with spin-orbit coupling (SOC) for the optimized cells, as well as slightly expanded and contracted versions (scaled by ±0.5% linearly). These calculations yielded the electron densities, kinetic energy densities, wave functions, and Kohn-Sham potential components needed for CP analysis. For consistency with VASP calculations, DFT-CP schemes were also repeated in ABINIT with GGA exchange-correlation functionals and can be found in the Supporting Information.

**Phonon Calculations.** The phonon band structures of the  $\alpha$ - and  $\beta$ -forms of  $\operatorname{Au_2BiP_2}$  were calculated with LDA-DFT using ABINIT in the framework of density functional perturbation theory, without spin—orbit coupling being included. A comparison of total energy with (DFT-CP) and without (phonon calculations) spin—orbit coupling can be found in Table S32. After the calculation of the self-consistent ground state and derivatives of the band energies with respect to k, phonon response calculations were carried out for q-points corresponding to each of the k-points in the irreducible wedge of the Brillouin zone. The responses were then collected into a database with the mrgddb utility, from which interatomic force constants, phonon density of states, and phonon band energies were determined with the anaddb utility. Phonon band structures, density of states distributions, and representations of the phonon modes at the  $\Gamma$  point are provided in the Supporting Information.

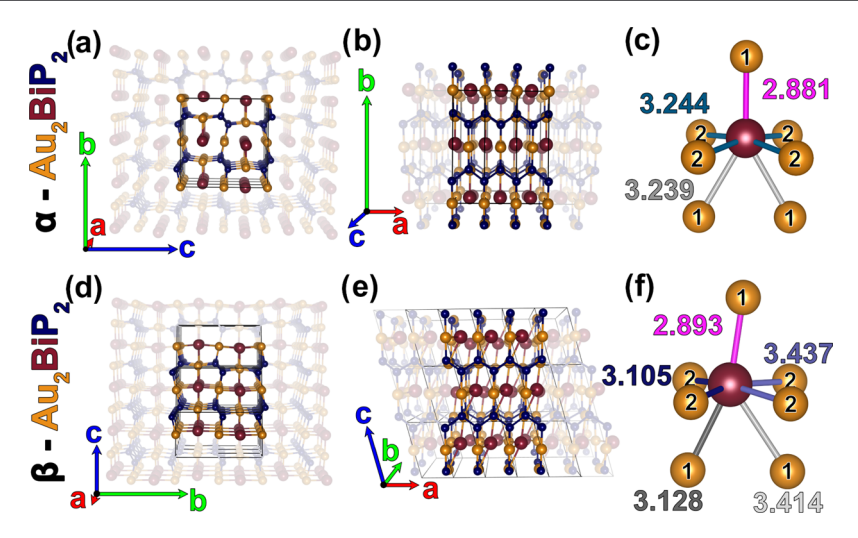


Figure 2.  $Au_2BiP_2$  crystal structures and their respective Bi coordination environments obtained through single-crystal X-ray diffraction studies. (a–c) Orthorhombic phase that is isotypic to  $Au_2TlP_2$ ,  $Au_2PbP_2$ , and  $Au_2Pb_{0.53}Bi_{0.43}P_2$ . (d–f) Monoclinic polymorph of  $Au_2BiP_2$  unique to M = Bi. Contact distances (Å) in panels (c) and (f) are given for  $Au_2BiP_2$  in the α- and β-phase, respectively.

**DFT Calculations.** Electronic band structures and density of states (DOS) distributions were performed using the Vienna Ab-initio Simulation Package (VASP). 44-46 For all phases in the  $\alpha$ -type structure, initial geometries were taken directly from the single-crystal structural solutions and relaxed, first with atomic movement within a fixed cell, followed by relaxation of all cell parameters. Like the relaxations using ABINIT, optimized geometries obtain small deviations from experimentally determined structures, the coordinates of which are listed in Tables S21-S25. Self-consistent calculations employed the generalized gradient approximation and the projector augmented wave potentials provided with the package 47,48 with Tl, Pb, and Bi semicore d orbitals treated as part of the valence set. For Au<sub>2</sub>Pb<sub>0.53</sub>Bi<sub>0.43</sub>P<sub>2</sub> only, the virtual crystal approximation method was used in conjunction with basis sets that did not include the Pb and Bi d orbitals to avoid errors associated with this approximation's treatment of semicore states. 49 All calculations also accounted for spin-orbit coupling. To obtain a convergence of 0.1 meV for all lphaphases in the primitive geometry, a  $\Gamma$ -centered 34  $\times$  34  $\times$  17 k-point mesh and energy cutoff of 520 eV was utilized. Calculations for  $\beta$ -Au<sub>2</sub>BiP<sub>2</sub> were treated with the same relaxation procedure. For hypothetical " $\beta$ -Au<sub>2</sub>TlP<sub>2</sub>" and " $\beta$ -Au<sub>2</sub>PbP<sub>2</sub>," only the cell volume was relaxed for reasons described in the main text. All single point and density of state calculations for the  $\beta$  phases were initially converged using a  $\Gamma$ -centered 48  $\times$  13  $\times$  26 k-point mesh and energy cutoff of 520 eV. The sumo package<sup>50</sup> was used to plot band structure diagrams.

**Electronic Transport.** Alternating current electronic transport measurements were performed by using a Quantum Design Physical Property Measurement System. Gold wires were connected in a four-probe geometry using conducting silver paste (Dupont 4929N) to small (approximately  $1000 \times 300 \times 400 \ \mu \text{m}^3$ ) needle-like single crystals. The crystallographic axes for the transport measurements were determined from the morphology of the crystals and alignment in SCXRD. For Hall and magnetoresistance measurements, data was taken at each temperature, sweeping from -9 to 9 T in 181 steps. For two-band fitting, the data for Hall resistivity and magnetoresistivity were antisymmetrized and symmetrized, respectively.

# ■ RESULTS AND ANALYSIS

**Structural Characterization.** Initial powder X-ray diffraction patterns for  $Au_2TlP_2$ ,  $Au_2PbP_2$ , and  $Au_2Pb_{0.53}Bi_{0.43}P_2$  indicate that the primary phase resides in the  $Au_2PbP_2$  structure type (i.e., the orthorhombic  $\alpha$ -phase). In contrast, synthesized  $Au_2BiP_2$  samples show a subtle difference compared to the remaining compounds in the series. The

pattern, shown in Figure S1, contains additional peaks around  $\sim$ 29°, which deviate from the orthorhombic phase. Additionally, there are peak splittings that are unobserved in the other samples. The magnitude of peak splitting is systematic; larger peak offsets occur at larger values of  $2\theta$ , indicating that this diffraction pattern belongs to a related structure type with slightly different lattice parameters. Still, this does not preclude the possibility that the sample also contains the  $\alpha$  phase, as many peaks can be attributed to this phase. The powder X-ray diffraction patterns of all samples studied here suffer from impurity phases stemming from leftover flux. In addition, the high absorption of constituent elements provides poor statistics and precludes us from drawing any meaningful conclusions via refinement of this powder X-ray data.

To better isolate and characterize the phases in this series, we turned to single-crystal X-ray diffraction. Structural solutions for Au<sub>2</sub>TlP<sub>2</sub>, Au<sub>2</sub>PbP<sub>2</sub>, Au<sub>2</sub>Pb<sub>0.53</sub>Bi<sub>0.43</sub>P<sub>2</sub>, and a few crystals within Au<sub>2</sub>BiP<sub>2</sub> are consistent with the reported space group Cmcm, and we did not see any evidence of structural distortions or modulations. Both Au<sub>2</sub>Pb<sub>0.53</sub>Bi<sub>0.43</sub>P<sub>2</sub> and Au<sub>2</sub>BiP<sub>2</sub>. were previously unreported in this structural family. Notably, for the Tl analogue, we significantly improved the quality of the refinement compared to the previous report.<sup>22</sup> The published structural solution required multiple Wyckoff positions with large anisotropies to refine the Tl position, and non-negligible residual electron densities  $(8.8/-7.5 \text{ e/Å}^3)$ remained. Utilizing a singular Wyckoff position for Tl, we observe a significant decrease in the absolute value of residual electron densities  $(2.41, -1.72 \text{ e/Å}^3)$ . These electron residuals are still large but considered negligible due to Fourier truncation errors in heavier atoms of Au and Tl. This also implies that the previous refinement for Au<sub>2</sub>HgP<sub>2</sub>, which suffered from similar issues, might similarly be solvable with only one Wyckoff site in the  $\alpha$ -phase. We believe that the previous results were affected by the applied acid etching procedure of the crystals or their sensitivity to air rather than ionic movement or a CDW.

If the previously reported Hg analogue also fits into the  $\alpha$  structure type, then the discovery of  $\alpha$ -Au<sub>2</sub>BiP<sub>2</sub> makes this structure surprisingly robust. The highly anisotropic structure would remain isotypic across four different valence electron configurations. But why? Our suspicion is that the approximate

atomic energy match of M and Au atomic orbital energies, compared to other elements (e.g., elements with 5p valence electrons), plays a role that allows significant charge transfer to the surrounding [Au<sub>2</sub>P<sub>2</sub>] framework, allowing this structural family to be robust toward chemical substitutions across M = Hg, Tl, Pb, and Bi. Using the Bi coordination environment in  $\alpha$ -Au<sub>2</sub>BiP<sub>2</sub> (Figure 2c) as an example, the Bi atom is coordinated by seven Au atoms—three Au1 contacts in the ab plane, of which one has a distance of 2.881 Å, and two have a distance of 3.240 Å, as well as four equidistant contacts to the Au2 atom, located in the ac plane, at a distance of 3.244 Å.

The shortest Au–M contact at 2.893 Å seems to be the most unique in the  $\alpha$  structural family. In molecular chemistry, a number of groups have isolated organometallic clusters with singular Au–Bi bond lengths ranging from 2.82 to 2.89 Å. <sup>51–53</sup> Notably, Ke and Gabbai perform a natural bond order analysis on  $[(o-(iPr_2P)C_6H_4)_2BiCl]AuCl$  (iPr=isopropyl group), showing non-negligible  $6s(Bi) \rightarrow 6s(Au)$  charge transfer in addition to the anticipated  $5d(Au) \rightarrow 6p(Bi)$  bonding. This casts doubt on the Bi atom in  $Au_2BiP_2$  having a neutral oxidation state. Under the suspicion that Bi could be oxidized by the surrounding framework, we sought to understand more broadly the role of charge transfer within the M coordination environment in the  $Au_2MP_2$  series.

Indeed, Bader charge analysis (Tables \$33-\$35) reveals that cationic M and P are charge-balanced by anionic Au, in line with the strong electronegative tendency of Au. While unusual, such negative oxidation states have been documented previously when coupled to extremely electropositive elements or liquid ammonia.<sup>54</sup> The short Au–Au distances (~3.25 Å) may indicate some amount of aurophilic interaction; however, aurophilic interactions are known only for Au(I) complexes.  $^{55-59}$  As the interactions in the  $\mathrm{Au_2MP_2}$  series are proposed to be between slightly anionic Au ions, it would be highly unusual for the interactions to be aurophilic, although we cannot rule out this possibility. Additionally, this analysis shows that the cationic M behavior is increased from Tl (+0.1814) through Pb (+0.3616) to Bi (+0.4743), with a corresponding increase in anionic behavior for atoms comprising the [Au<sub>2</sub>P<sub>2</sub>] framework throughout this series. Thus, we suggest that this  $M \to [Au_2P_2]$  charge redistribution in the Au<sub>2</sub>MP<sub>2</sub> series is the key to accommodating the breadth of valence electrons in this series as well as preventing distortions in the structure.

Sampling many crystals via single-crystal X-ray diffraction, we found that Au<sub>2</sub>BiP<sub>2</sub> exists in two different structures: the aforementioned orthorhombic C-centered cell analogous to the rest of the structural family and a primitive monoclinic structure, which is seen predominantly in all samples. Initial unit cell refinement for the  $\beta$ -phase finds a monoclinic space group with lattice parameters a = 3.25 Å, b = 11.26 Å, c = 5.898Å, and  $\beta = 105.066^{\circ}$ . Reconstructed precession images in h0l (monoclinic) and analogous hk0 (orthorhombic) are shown in Figure 3. Although very similar, a slight displacement in the peak positions reveals a distinction between the orthorhombic (Figure 3a) and monoclinic (Figure 3c) phases. Forcing the monoclinic pattern into indexation of the orthorhombic cell, as shown in Figure 3b, shows that expected peak positions, given by intersections of the white grid, in the "hk0" plane would intersect observed peaks better by broadening the angle between  $a^*$  and  $b^*$ . The cell reflecting the broadened angle clearly describes the points better, and the need to index as a monoclinic cell (Figure 3c) becomes apparent. In addition, 58

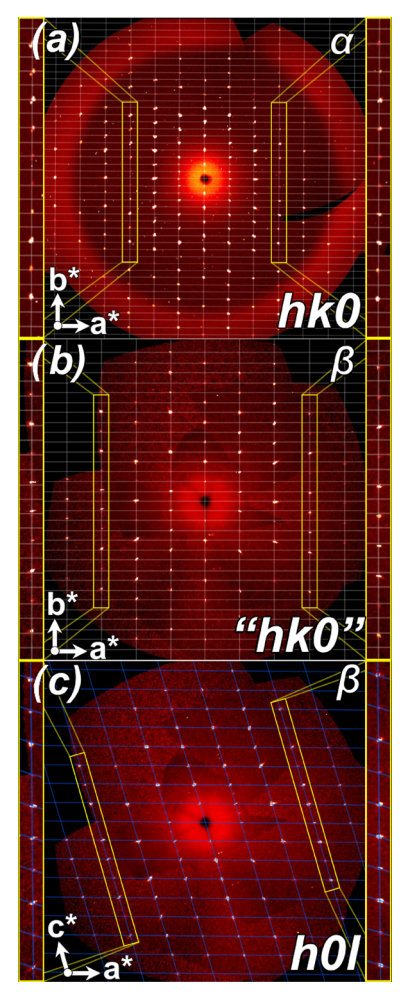


**Figure 3.** Reconstructed precession images from single-crystal X-ray diffraction for both polymorphs of Au<sub>2</sub>BiP<sub>2</sub>, with the specific polymorph type labeled in the top right of each image. Overlaid reciprocal lattice grids are shown for the orthorhombic (white) and monoclinic (blue) unit cells. (a) *hk*0 reconstruction from an orthorhombic crystal correctly indexed in the orthorhombic *C*-centered unit cell. (b) Data from a monoclinic crystal incorrectly indexed in the orthorhombic *C*-centered unit cell. Intensities seen above (inset, left) and below (inset, right) the white grid lines are consistent with a monoclinic distortion. (c) *h0l* reconstruction from a monoclinic crystal indexed in the correct monoclinic setting. The reciprocal lattice of the monoclinic cell here is consistent with the observed intensities.

out of the first 59 picked monoclinic crystals appear twinned  $180^{\circ}$  along the crystallographically unique *b*-axis (Figure S11), confirming the difference to the orthorhombic phase, which has no tendency to twin along its analogous *c*-axis.

Using reconstructed precession images to decipher the  $\beta$ -phase space group, reflection conditions k=2n along the 0k0 direction narrowed the choice down to either space group  $P2_1/m$  and  $P2_1$ . Integration and refinement in these space groups were more consistent with  $P2_1/m$ , resulting in a final  $R^2$  ( $I>3\sigma$ ) of 3.04 and S ( $I>3\sigma$ ) of 1.4588. Further justification of this choice of space group can be found in the Supporting Information. The  $\beta$  phase appears similar to the  $\alpha$  phase when looking down the tunnel axis ( $\alpha$  and  $\alpha$  crystallographic axes for the  $\alpha$  and  $\alpha$  cells, respectively (Figure 2a,d)). However, a noticeable change can be seen when looking perpendicular to the chain direction (Figure 2b,e). In the monoclinic cell, the Bi

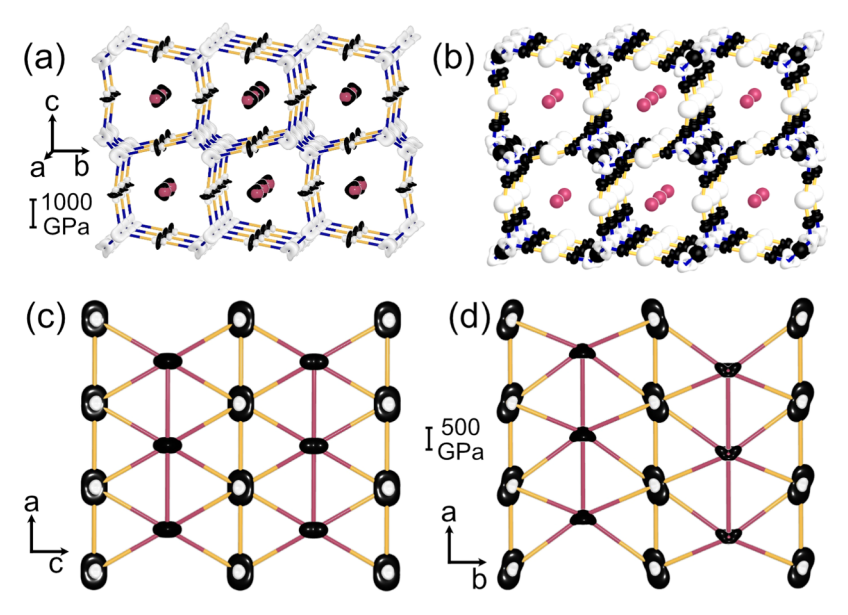


Figure 4. Chemical pressure analysis of  $Au_2BiP_2$  and its polymorphism. (a) CP scheme for the  $\alpha$ -form viewed approximately down the [100] direction. The CP distribution around each atom is represented with a radial plot, with the sizes of the lobes being proportional to the magnitude of the sum of the pressure contributions along that direction. The color of the lobes gives the sign of the pressure: black for negative, white for positive. (b) Isosurfaces of the CP map. White: isosurface for a positive value. Black: isosurface for a negative value of equal magnitude. (c-d) CP schemes plotted for cross sections through the Bi-filled channels in the (c) orthorhombic and (d) monoclinic polymorphs.

chain has a translational shift through the tunneled framework by  $\sim$ 0.27 Å compared with the  $\alpha$ -phase (Figure 2c,f). The translation of Bi atoms is in the same direction within each tunnel; however, the direction of translation is flipped in adjacent tunnels.

To gain some insight into why the  $\beta$  phase appears more frequently, we again turn to the Bi coordination environment. Similar to the  $\alpha$ -phase, the  $\beta$ -phase also features a short Au–Bi contact (2.893 Å) (Figure 2f). However, as a consequence of the translational Bi-shift, the two Au1, formally equidistant contacts, have skewed to a short and long contact measuring 3.127 and 3.414 Å. Likewise, the Bi-Au2 contacts undergo a similar change with two contacts each at 3.105 and 3.437 Å (Figure 2f). Additionally, upon comparison of the  $\alpha$  and  $\beta$ phases, Bader charge analysis indicates an increased charge transfer between the Bi-Au2 contacts at the slight expense of the lengthened Bi-Au1 contact. Therefore, we suspect that this structural distortion to the  $\beta$ -type Au<sub>2</sub>BiP<sub>2</sub> is stabilized through these additional interactions. Additionally, the empirical atomic radii of Tl (1.90 Å) and Pb (1.80 Å) are significantly larger than that of Bi (1.60 Å). It is feasible, then, to imagine the bulkier Tl and Pb atoms have to pay an energetic fee when translating along the chain axis. Thus, determining the origin of the  $\beta$ -phase stability requires computation. For this, we turn to a series of density functional theory (DFT) calculations, starting with DFT-chemical pressure (DFT-CP) analysis, which investigates the conflicts within atomic packing arrangements. Afterward, we turn to electronic factors associated with band structure and density of states computations.

Chemical Pressure Analysis. DFT-CP analysis provides a context for understanding the observed polymorphism of Au<sub>2</sub>BiP<sub>2</sub> (Figure 4a). CP analysis probes local packing tensions along atomic contacts in a unit cell. To do this, self-consistent calculations with slightly contracted and expanded unit cells are computed. Examination of how a given atom's energy changes with respect to the perturbed volumes are described as

pressures that inform whether the atoms would like its environment to shrink (negative pressure, black lobes) or expand (positive pressure, white lobes) along a given atom—atom contact. A prominent feature of both the  $\alpha$ - and  $\beta$ -polymorphs of this compound is the Au–P network, whose 1D open channels accommodate the Bi atoms. In the CP scheme, the Au–P and P–P contacts building this network exhibit positive CPs, indicating that the Au–P sublattice is overly contracted. The expansion of the structure is prevented, however, by negative CPs along Au–Au contacts in the orthorhombic a-direction, as well as the Au atom's interactions with the Bi atoms. Overall, this scheme creates the impression of an Au–P framework holding open large voids for occupation by the Bi atoms, which are not large enough to fill these spaces completely.

Origins of the apparent rigidity of the Au-P framework may be found by examining isosurfaces of the CP map (Figure 4b),60 which provide a visual representation of chemical bonding forces. In this representation, shells of positive pressure (white) appear around the Au and P atoms (particularly away from the Au-P and P-P interactions), corresponding to the energetic costs of distorting the atomic orbitals in the core regions of the atoms necessary for the formation of bonds. Along the Au-P and P-P contacts, however, peanut-shaped domains of negative pressure (black) appear near the bond midpoints. These features are highly reminiscent of the bonding regions in the CP maps obtained previously for the diamond form of C and other covalent solids.<sup>60</sup> Their distribution in tetrahedral and linear arrangements around the P and Au atoms, respectively, hints at sp<sup>3</sup> and sp hybridization. Contributions to the electron density from bands containing significant P character, shown in Figure S15, are consistent with this bonding scheme. The bonding within the open Au<sub>2</sub>P<sub>2</sub> tunnel framework may thus be considered as highly covalent.

Let's now consider how the Bi atoms, arranged into chains, fit into this framework. In the CP scheme for the  $\alpha$  form

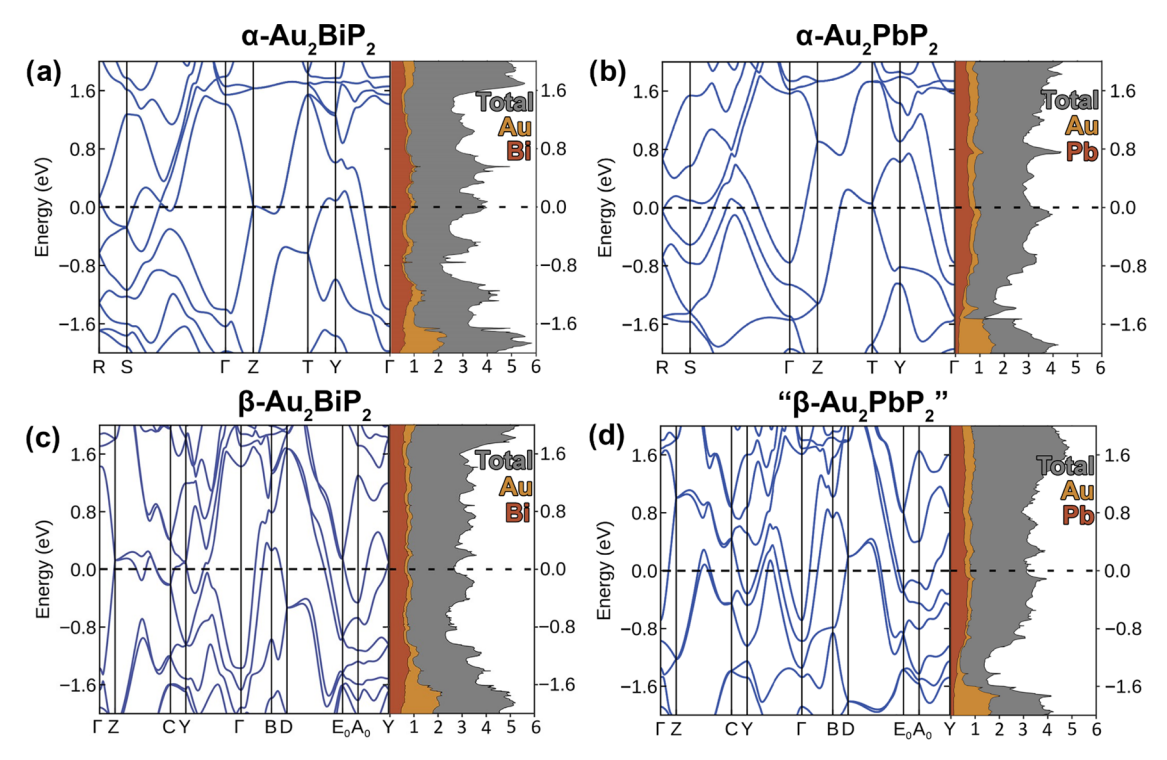


Figure 5. DFT Band structure and density of states calculations for (a)  $\alpha$ -Au<sub>2</sub>BiP<sub>2</sub>, (b)  $\alpha$ -Au<sub>2</sub>PbP<sub>2</sub>, (c)  $\beta$ -Au<sub>2</sub>BiP<sub>2</sub>, and (d) a hypothetical " $\beta$ -Au<sub>2</sub>PbP<sub>2</sub>." Partial densities of states are shaded red for Pb and Bi contributions and gold for Au contributions. Shaded regions are individually plotted and not summed such that Au contributions are generally larger than Bi. The large density of states at the Fermi energy in panel (a) consists of states near the Z point and is exclusive to  $\alpha$ -Au<sub>2</sub>BiP<sub>2</sub> in the series.

(Figure 4a), Bi appears with a triangular distribution of negative CP, reflective of overly extended contacts to the Au atoms in the surrounding framework. The Au<sub>2</sub>P<sub>2</sub> framework thus appears to hold open void spaces that are too large for the Bi atoms to completely fill. The looseness of this packing creates an opportunity for mobility of the Bi atoms within the Au-P channels as they seek to minimize their local pressures. At the same time, the shapes of the CP distributions are least negative along the Bi-Bi chain axis. Their spacing along lattice direction a is evidently close to ideal in this arrangement, and in their motions, the Bi atoms would likely prefer to gain shorter distances to the channel walls (i.e., toward either of the Au2 positions) than undergo a Peirels distortion along the chain. This feature is consistent with the observation that in the transition to the  $\beta$  form, each Bi chain moves together as a group and also supports the idea that the guest M atoms rattle within the host Au<sub>2</sub>P<sub>2</sub> framework.

In Figure 4c,d, we explore how the packing situation changes as the structure goes from the  $\alpha$  polymorph to the  $\beta$  form, which is most easily seen by examining an ac-cross section through the channel in the former and the corresponding plane in the latter (the ab-plane, in the monoclinic setting). In the orthorhombic  $\alpha$  structure, Bi atoms are positioned at highly symmetric sites, each evenly spaced between four Au atoms in the plane. In this configuration, the Bi atom is 3.22 Å (corresponding to the LDA-DFT optimized geometry) from all four Au atoms (Figure 4c). Negative CP is evenly distributed across these Bi-Au interactions. On moving to the monoclinic  $\beta$  form, the major change is that neighboring Bi chains move alternatively up and down along a by about 0.4 Å. The resulting Bi coordination environment leaves two Au atoms closer at 3.04 Å and two Au atoms farther away at 3.47 Å (Figure 4d). While the two longer Au–Bi contacts slightly increase in negative pressure, the two shorter contacts have noticeably reduced negative pressure. Indeed, the net atomic pressure on the Bi atoms decreases from -118.48 GPa in the orthorhombic structure to -101.79 GPa in the monoclinic form

While the Au<sub>2</sub>P<sub>2</sub> framework appears structurally to be relatively unperturbed by this transformation, the CP schemes point to a subtle effect. The Au atoms in the structure experience CP distributions with positive and negative CP lobes running perpendicular to each other, such as the positive and negative lobes of a d orbital. Such quadrupolar (QP) CP distributions are suggestive of a high propensity to exhibit lowfrequency phonon modes, wherein the Au atoms have easy motion along directions of negative pressure, e.g., in and out of the Bi-filled voids. In fact, the quadrupolar (QP) metric values<sup>61</sup> calculated for these sites (0.844 and 0.830 in the monoclinic type and 0.862 and 0.843 in the orthorhombic type) are among the highest thus far documented. For the orthorhombic structure, the direction of the largest negative CP (and thus the softest motion) for the Au atoms is along the a-axis. In the monoclinic structure, the shift of the Bi chain influences this arrangement. The primary axis of the negative pressure on the Au atoms tilts slightly from the a-axis to align with the stretched Au-Bi contact. The phase transition thus hints at the possibility of imaginary phonon frequencies in the α-Au<sub>2</sub>BiP<sub>2</sub> structure type. Comparison of the phonon band structure, density of states, and representations of phonon modes of  $\alpha$ - and  $\beta$ -Au<sub>2</sub>BiP<sub>2</sub>, shown in Figures S16–S18, reveal a branch with imaginary frequencies in the  $\alpha$ -type dispersion that are resolved when transitioning to the  $\beta$ -type structure. Thus, the  $\alpha$ -phase is indeed dynamically unstable relative to displacements toward the  $\beta$ -phase geometry.

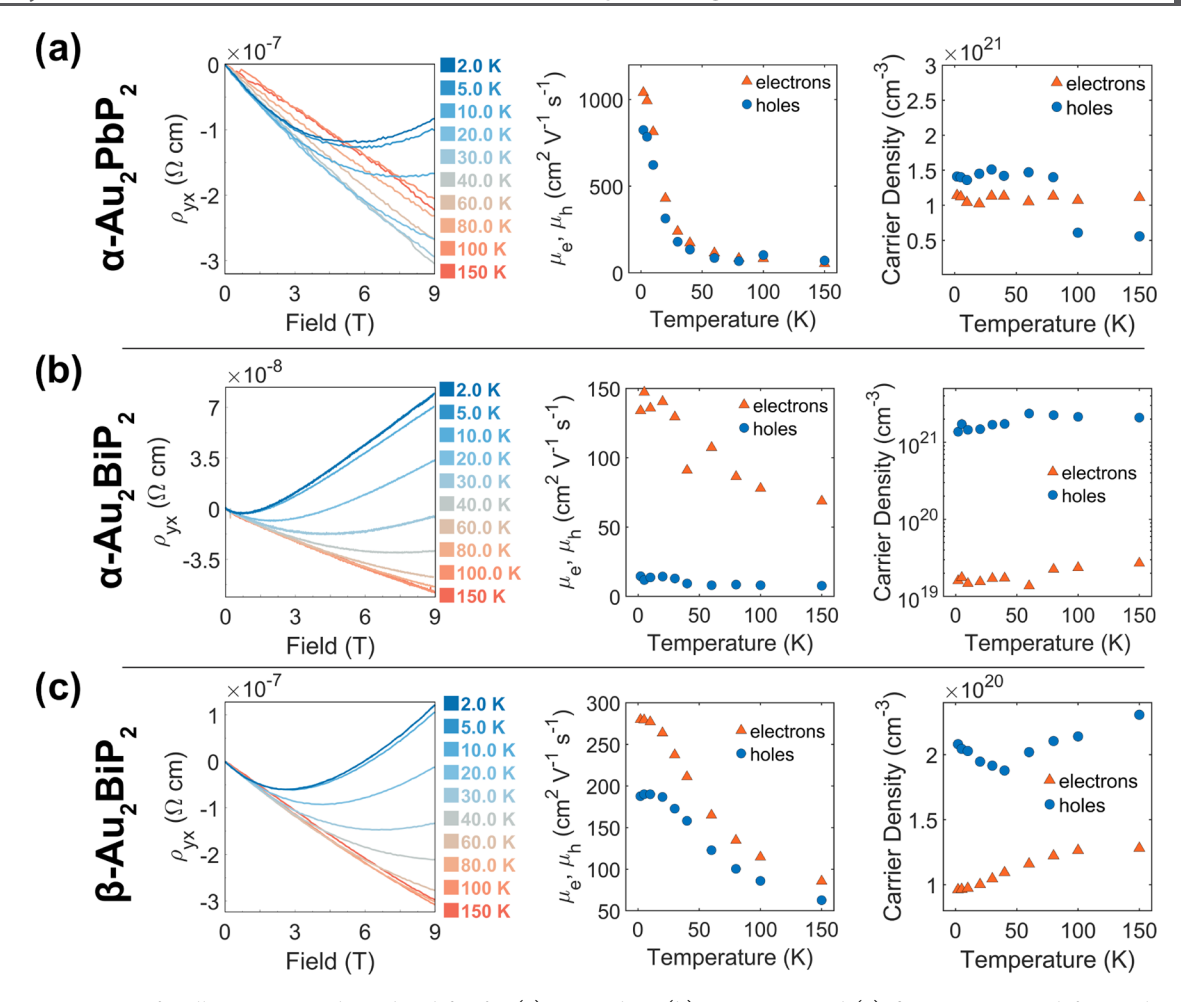


Figure 6. Comparison of Hall resistivity and two-band fits for (a)  $\alpha$ -Au<sub>2</sub>PbP<sub>2</sub>, (b)  $\alpha$ -Au<sub>2</sub>BiP<sub>2</sub>, and (c)  $\beta$ -Au<sub>2</sub>BiP<sub>2</sub>. From left to right: transverse (Hall) resistivity showing nonlinear signal due to multiple carriers, fit values of charge carrier mobilities as a function of temperature, and fit values of charge carrier densities as a function of temperature. Carrier densities in  $\alpha$ -Au<sub>2</sub>BiP<sub>2</sub> are plotted on a logarithmic scale.

**DFT Calculations.** In addition to imaginary phonon mode minimization, we also suspected the structural distortion of  $\beta$ -Au<sub>2</sub>BiP<sub>2</sub> to be electronically driven. DFT calculations utilizing Perdew-Burke-Ernzerhof (PBE) pseudopotentials are also in agreement with the experimental observation that the Bi analogue forms preferentially in the  $\beta$ -phase. Self-consistent calculations for the  $\beta$ -phase reach a total energy convergence of -23.1927 eV per formula unit (fu), while calculations for the lpha-phase converge at -23.1858 eV/fu. The small 6.9 meV/fu difference in energy supports the observation that the monoclinic phase is the dominant phase, but as the energy difference is very small, Au<sub>2</sub>BiP<sub>2</sub> can also crystallize in the orthorhombic structure. A similar result is produced in identical calculations with unrelaxed geometries; however, slight deviations arise when using local density approximation (LDA) pseudopotentials. The most significant deviation is that LDA calculations put  $\alpha$ -Au<sub>2</sub>BiP<sub>2</sub> as being slightly energetically favorable. Both of these methods confirm that both  $\alpha$ - and  $\beta$ -Au<sub>2</sub>BiP<sub>2</sub> are extremely close in energy, with PBE functionals matching our experimental observations. We also theoretically investigated whether hypothetical  $\beta$ -type "Au<sub>2</sub>TlP<sub>2</sub>" and "Au<sub>2</sub>PbP<sub>2</sub>" could exist. For this, we took our structural solution for  $\beta$ -Au<sub>2</sub>BiP<sub>2</sub> and swapped the Bi atom for Tl or Pb as the calculation input. However, by allowing ionic relaxation, these atoms converge to their positions in the  $\alpha$ type. If we instead prohibit ionic relaxation and relax only

volume parameters, self-consistent calculations converge, with the  $\alpha$  phase being favored by 33.2 (Tl) and 23.2 (Pb) meV/fu.

To better understand the mechanism of the structural distortion toward the  $\beta$  phase, we compare the density of states distributions and band structures of  $\alpha$ -Au<sub>2</sub>BiP<sub>2</sub>,  $\alpha$ -Au<sub>2</sub>PbP<sub>2</sub>,  $\beta$ -Au<sub>2</sub>BiP<sub>2</sub>, and our hypothetical "β-Au<sub>2</sub>PbP<sub>2</sub>" (Figure 5a-d). In comparing the band structure and density of states of the two Au<sub>2</sub>BiP<sub>2</sub> polymorphs (Figure 5a,c), we see that the Fermi level of the  $\alpha$  phase falls squarely on a nonsymmorphically enforced band degeneracy at the Z point. Reconstructed partial charge density for this degeneracy, shown in Figure S14, demonstrates the Au d<sub>2</sub> and Bi p<sub>2</sub> orbital contributions in this half-filled, doubly degenerate band. This makes sense in the light of a formally half-filled Bi-p-shell, as such band degeneracies are a consequence of band folding, and half-filling is required to place the Fermi level as the degenerate point. 62,63 As other bands are crossing the Fermi level as well, this nonsymmporphic degeneracy can be partially stabilized. However, some instability is indicated by the rather small dispersion of the band along the  $Z \rightarrow T$  direction, which appears to be the consequence of avoidance of crossing below the Fermi energy along this path. If we compute the band structure in the conventional orthorhombic C-centered cell (Figure S13), the lack of dispersion becomes more evident along paths  $T \rightarrow Z_1$ ,  $\Gamma \rightarrow Y_1$ ,  $Y \rightarrow \Gamma$ , and  $Z \rightarrow T$ . Those bands in  $\alpha$ -Au<sub>2</sub>BiP<sub>2</sub> constitute the large peak in the density of states (DOS) that

partial DOS calculations confirm are predominantly of Au d and Bi p orbital contributions. The peak in the DOS indicates a slight electronic instability. The fact that this peak stems from Au d and Bi p orbitals suggests that the charge transfer in the  $\alpha$ -phase is not sufficient to fully relieve the electronic stress of this half-filled band. Comparatively, in  $\beta$ -Au<sub>2</sub>BiP<sub>2</sub>, the peak in the DOS is no longer present, which is evident by the pseudogap at the Fermi level. This agrees with the Bader charge analysis, suggesting that the monoclinic distortion increases the charge transfer, thus removing charge from Bi and moving the system further away from the undesired half-filling.

In contrast to the Bi phases, the band structure of  $\alpha$ -Au<sub>2</sub>PbP<sub>2</sub> contains no bands with low dispersion that could form a peak in the DOS near the Fermi energy, and the transition to the hypothetical "β-Au<sub>2</sub>PbP<sub>2</sub>" does not form a pseudogap; instead, nearly identical density of states can be seen at the Fermi level. This indicates that for the smaller valence electron count for M = Pb, the charge transfer that is already facilitated in the  $\alpha$ -phase is sufficient to stabilize the structure, rendering the transition to  $\beta$  unnecessary. The same then explains the observation of only the  $\alpha$ -phase for M = Hg and Tl. To see how unique the  $\beta$ -phase is to a valence electron count of 5 per M, we synthesized a mixed phase between Pb and Bi, Au<sub>2</sub>Pb<sub>0.53</sub>Bi<sub>0.43</sub>P<sub>2</sub>. For that exact composition, we can also only find the  $\alpha$ -phase, which shows how narrow the valence electron count is for the additional instability to occur. Only when the Fermi level is very close to a peak in the DOS, the  $\beta$ -phase can be expected. Unfortunately, due to the radioactivity of Po, we could not test whether the valence electron count could be increased beyond M = Bi. Synthesis attempts with any fifth-row p-block metals, including In, Sn, Sb, and Te, were all unsuccessful.

**Electronic Transport Measurements.** To examine how the calculated electronic structure manifests itself in observable properties, we probed the electronic transport of  $\alpha$ -Au<sub>2</sub>PbP<sub>2</sub>,  $\alpha$ -Au<sub>2</sub>BiP<sub>2</sub>, and  $\beta$ -Au<sub>2</sub>BiP<sub>2</sub>. As discussed in the DFT section, those three compounds have significant variations in their electronic structure close to the Fermi level:  $\alpha$ -Au<sub>2</sub>PbP<sub>2</sub> contains many disperse bands,  $\alpha$ -Au<sub>2</sub>BiP<sub>2</sub> hosts states that are nondisperse, but these states are gapped out in  $\beta$ -Au<sub>2</sub>BiP<sub>2</sub>.

The temperature dependence of the linear resistivity  $(\rho_{xx})$ for  $\alpha$ -Au<sub>2</sub>PbP<sub>2</sub> (Figure S21),  $\alpha$ -Au<sub>2</sub>BiP<sub>2</sub> (Figure S23), and  $\beta$ -Au<sub>2</sub>BiP<sub>2</sub> (Figure S25) with current parallel to the 1D chain shows that all three compounds are metallic, as expected. The residual resistivity ratios ( $\rho_{xx,300\text{K}}/\rho_{xx,1.8\text{K}}$ ) are ~4, ~2, and ~52, respectively, indicating that the  $\beta$ -phase might have fewer defects. The needle-like morphology of the crystals precludes the measurement of  $\rho_{yy}$  or  $\rho_{zz}$ . In the case of  $\alpha$ -Au<sub>2</sub>PbP<sub>2</sub>, some samples show a broad transition in  $\rho(T)$  at  $T \sim 70$  K that remains unaltered up to the highest applied magnetic field (9 T). The insensitivity of the transition to the magnetic field suggests that this transition is possibly related to a structural distortion and/or formation of a CDW; however, no clear distortion is observed in SCXRD precession data taken at 15 K (see the SI for more information). As this transition does not appear in every sample, it might stem from an impurity, and further work to elucidate its origin is necessary. No such transitions are observed in either  $Au_2BiP_2$  phase above T = 1.8

To determine the mobility of the charge carriers, we performed magnetoresistance  $(\rho_{xx}(B))$  and Hall resistivity  $(\rho_{vx}(B))$  measurements on single crystals of  $\alpha$ -Au<sub>2</sub>PbP<sub>2</sub>,  $\alpha$ -

Au<sub>2</sub>BiP<sub>2</sub>, and  $\beta$ -Au<sub>2</sub>BiP<sub>2</sub> with the current along the linearchain-axis and magnetic field applied perpendicular to the chain-axis. A nonlinear magnetic field dependence of the Hall response is observed at low temperatures for all three crystals, shown in the left panel of Figure 6a–c, which usually hints at multiple charge carrier types contributing to conductance.

Furthermore, in all three band structures for  $\alpha$ -Au<sub>2</sub>PbP<sub>2</sub>,  $\alpha$ -Au<sub>2</sub>BiP<sub>2</sub>, and  $\beta$ -Au<sub>2</sub>BiP<sub>2</sub> (Figure 5a–c), we observe both hole and electron pockets, confirming our suspicion that multiple charge carriers are present in these systems. In an attempt to deconvolute the number and mobility of these charge carriers, we turn to a standard two-band model to simultaneously fit the field dependence of the transverse and longitudinal conductivity, with eqs 1 and 2 below.

$$\sigma_{yx} = \left[ \frac{n_{h}\mu_{h}^{2}}{1 + (\mu_{h}\mu_{0}H)^{2}} - \frac{n_{e}\mu_{e}^{2}}{1 + (\mu_{e}\mu_{0}H)^{2}} \right] e\mu_{0}H$$
(1)

$$\sigma_{xx} = e \left[ \frac{n_{\rm h} \mu_{\rm h}}{1 + (\mu_{\rm h} \mu_{\rm 0} H)^2} + \frac{n_{\rm e} \mu_{\rm e}}{1 + (\mu_{\rm e} \mu_{\rm 0} H)^2} \right]$$
(2)

Here,  $\sigma_{xy} = \frac{-\rho_{yx}}{\rho_{yx}^2 + \rho_{xx}^2}$ ,  $\sigma_{xx} = \frac{\rho_{xx}}{\rho_{yx}^2 + \rho_{xx}^2}$ ,  $n_h$  ( $n_e$ ), and  $\mu_h$  ( $\mu_e$ ) are defined as the hole (electron) carrier density and mobility, respectively.

The two-band model works well in describing the Hall conductivity for  $\alpha$ -Au<sub>2</sub>PbP<sub>2</sub>. At 2 K, our model indicates a hole concentration of  $1.41 \times 10^{21}$  cm<sup>-3</sup> as well as an electron carrier concentration of  $1.14 \times 10^{21}$  cm<sup>-3</sup>. The slightly larger hole concentration stems from the large hole pockets seen in the band structure (Figure 5b) centered around the S and  $\Gamma$ points. The slightly smaller electron carrier concentrations are expected from electron pockets observed along paths  $S \to \Gamma$ , Z  $\rightarrow$  T, and  $T \rightarrow Y \rightarrow \Gamma$ . In general, the carrier concentrations agree with the metallic nature of the samples. As mentioned previously, the band structure of  $\alpha$ -Au<sub>2</sub>PbP<sub>2</sub> contains highly dispersed bands. Given the proximity of the Fermi level to the center of these disperse bands, where the effective electron mass is lowest, we expect this system to have the highest charge-carrier mobilities of the three compounds studied. Indeed, at 2 K, the hole and electron mobility are 824.3 and  $1037.3 \text{ cm}^2/(\text{V s})$ , respectively.

Fits for  $\alpha$ -Au<sub>2</sub>BiP<sub>2</sub> result in a hole density of  $1.72 \times 10^{21}$  and electron density of  $1.76 \times 10^{19}$  cm<sup>-3</sup>. The mobility values are 11.9 and 147.2 cm<sup>2</sup>/(V s) for holes and electrons, respectively. These slower mobilities, as compared with  $\alpha$ -Au<sub>2</sub>PbP<sub>2</sub>, correlate well with the less disperse bands near the Fermi energy in  $\alpha$ -Au<sub>2</sub>BiP<sub>2</sub> (Figure 5a).

As expected from its band structure,  $\beta$ -Au<sub>2</sub>BiP<sub>2</sub> shows differences in charge transport from both  $\alpha$ -type structures studied. After a similar two-band fit, we obtain the hole and electron densities to be  $2.08 \times 10^{20}$  and  $9.58 \times 10^{19}$  cm<sup>-3</sup>, respectively. In comparison to  $\alpha$ -Au<sub>2</sub>BiP<sub>2</sub> ( $n_{\rm h} = 1.72 \times 10^{21}$ ), the hole density in  $\beta$ -Au<sub>2</sub>BiP<sub>2</sub> is nearly an order of magnitude lower ( $2.08 \times 10^{20}$ ). This agrees nicely with the fact that the peak in the DOS in  $\alpha$ -Au<sub>2</sub>BiP<sub>2</sub> is gapped out, creating a pseudogap, which reduces the carrier concentration. The mobility also slightly increases (doubles) in  $\beta$ -Au<sub>2</sub>BiP<sub>2</sub>, as compared with that in  $\alpha$ -Au<sub>2</sub>BiP<sub>2</sub>, which is expected when the flatter bands comprising the peak in the DOS are removed. Still, both Bi compounds have significantly lower mobilities than the Pb compound, which agrees with the band structure

predictions, as  $\alpha$ -Au<sub>2</sub>PbP<sub>2</sub> features the steepest bands, despite the low RRR, which suggests that scattering processes that hinder charge mobility are prevalent in this sample. Overall, the electronic transport measurements are in line with the predicted band structures and further corroborate the mechanism of polymorph formation in Au<sub>2</sub>BiP<sub>2</sub>.

## OUTLOOK

In this work, we reexamined single-crystal X-ray diffraction solutions and chemical bonding analysis of the ternary q1d Au<sub>2</sub>MP<sub>2</sub> family. In doing so, we found that we can extend this structural family to include the compositions of  $Au_2Pb_{0.53}Bi_{0.43}P_2$  and  $Au_2BiP_2$ . Single-crystal X-ray studies also demonstrated the lack of satellite peaks, indicating no CDW formation. Additionally, we found that Au<sub>2</sub>BiP<sub>2</sub> forms with two polymorphs: one phase in the orthorhombic Ccentered  $\alpha$  structure type common to M = Hg, Tl, and Pb but much more commonly observed as a secondary phase to a newly reported monoclinic form, with a new structure type. Utilizing DFT-chemical pressure analysis, we show that M atoms in the  $\alpha$ -type structure are not limited by the size of their radii throughout this series; rather, the [Au<sub>2</sub>P<sub>2</sub>] framework may benefit from a bulkier interstitial atom. Further DFT band structure and density of states calculations show that the exclusivity of the monoclinic  $\beta$ -phase to M = Bi is also due to an electronic minimization that is unrealized in other compositions in the orthorhombic  $\alpha$  structural family. We were also able to show how increasing the valence electron count will favor the  $\beta$ -phase. We then validate the predicted band structures utilizing electrical transport measurements to elucidate charge carrier densities and mobilities for  $\alpha$ - $Au_2PbP_2$ ,  $\alpha$ - $Au_2BiP_2$ , and  $\beta$ - $Au_2BiP_2$ , finding general good agreement with predicted band structures and measured differences in mobilities and carrier concentration. Overall, this study shows that 1D metallic chains can be stable in a large range of valence electron counts when there are noninnocent interactions between the tunnel framework that surrounds the chain. Structures will distort to relieve packing and electronic instabilities, as exemplified by our discovery of the  $\beta$ polymorph of Au<sub>2</sub>BiP<sub>2</sub>. When designing 1D systems in 3D crystals, potential packing frustrations and charge transfer with the tunnel structure should thus be carefully considered.

#### ASSOCIATED CONTENT

## **Supporting Information**

The Supporting Information is available free of charge at https://pubs.acs.org/doi/10.1021/acs.chemmater.4c00784.

Crystallographic Information Files have been deposited in the CCDC with deposition numbers CSD 2379816-2379820 (ZIP)

Check cif files (ZIP)

Elemental disperse spectroscopy for  $Au_2Pb_{0.53}Bi_{0.43}P_2$  and both  $Au_2BiP_2$  polymorphs, crystallographic model information, single-crystal diffraction precession images, computationally relaxed geometries, band structure calculations, partial charge density reconstructions, DFT-CP calculations, Bader charge analysis, and two-band fitting details (PDF)

#### AUTHOR INFORMATION

#### **Corresponding Author**

Leslie M. Schoop — Department of Chemistry, Princeton University, Princeton, New Jersey 08544, United States; orcid.org/0000-0003-3459-4241; Email: lschoop@princeton.edu

#### **Authors**

Scott B. Lee — Department of Chemistry, Princeton University, Princeton, New Jersey 08544, United States; ocid.org/0000-0003-0709-935X

Jonathan S. Van Buskirk — Department of Chemistry, University of Wisconsin—Madison, Madison, Wisconsin 08544, United States; © orcid.org/0000-0003-3347-3480

Fatmagül Katmer — Department of Chemistry, Princeton University, Princeton, New Jersey 08544, United States; orcid.org/0000-0003-1644-4725

Suchismita Sarker – CHESS, Cornell University, Ithaca, New York 14853, United States

Daniel C. Fredrickson – Department of Chemistry, University of Wisconsin—Madison, Madison, Wisconsin 08544, United States; orcid.org/0000-0002-3717-7008

Complete contact information is available at: https://pubs.acs.org/10.1021/acs.chemmater.4c00784

#### Notes

The authors declare no competing financial interest.

## ACKNOWLEDGMENTS

L.M.S. was supported by the NSF through NSF grant OAC-2118310 and NSF-MRSEC through the Princeton Center for Complex Materials DMR-2011750, as well as by the Gordon and Betty Moore Foundation's EPIQS initiative through Grant No. GBMF9064 and the David and Lucille Packard Foundation. S.B.L. was supported by the National Science Foundation Graduate Research Fellowship Program under Grant No. DGE-2039656. Any opinions, findings, and conclusions or recommendations expressed in this material are those of the author(s) and do not necessarily reflect the views of the National Science Foundation. J.S.V.B. and D.C.F. gratefully acknowledge the financial support from the National Science Foundation through Grant DMR-2127349. The authors acknowledge the use of Princeton's Imaging and Analysis Center (IAC), which is partially supported by the Princeton Center for Complex Materials (PCCM), a National Science Foundation (NSF) Materials Research Science and Engineering Center (MRSEC; DMR-2011750). Research conducted at the Center for High-Energy X-ray Science (CHEXS) was supported by the National Science Foundation (BIO, ENG, and MPS Directorates) under award DMR-1829070. L.M.S. would like to thank Roald Hoffmann for making her aware of this class of materials.

## REFERENCES

- (1) Petrović, A. P.; Ansermet, D.; Chernyshov, D.; Hoesch, M.; Salloum, D.; Gougeon, P.; Potel, M.; Boeri, L.; Panagopoulos, C. A disorder-enhanced quasi-one-dimensional superconductor. *Nat. Commun.* **2016**, 7, No. 12262.
- (2) Wang, P.; Yu, G.; Kwan, Y. H.; et al. One-dimensional Luttinger liquids in a two-dimensional moiré lattice. *Nature* **2022**, *605*, 57–62. (3) Chen, X.; Lu, X.; Deng, B.; Sinai, O.; Shao, Y.; Li, C.; Yuan, S.;

Tran, V.; Watanabe, K.; Taniguchi, T.; Naveh, D.; Yang, L.; Xia, F.

Widely tunable black phosphorus mid-infrared photodetector. *Nat. Commun.* **2017**, *8*, No. 1672.

- (4) Tan, L. B.; Cotlet, O.; Bergschneider, A.; Schmidt, R.; Back, P.; Shimazaki, Y.; Kroner, M.; Imamoğlu, A. Interacting Polaron-Polaritons. *Phys. Rev. X* **2020**, *10*, No. 021011.
- (5) Balandin, A. A.; Ghosh, S.; Bao, W.; Calizo, I.; Teweldebrhan, D.; Miao, F.; Lau, C. N. Superior Thermal Conductivity of Single-Layer Graphene. *Nano Lett.* **2008**, *8*, 902–907.
- (6) Wakeham, N.; Bangura, A. F.; Xu, X.; Mercure, J.-F.; Greenblatt, M.; Hussey, N. E. Gross violation of the Wiedemann-Franz law in a quasi-one-dimensional conductor. *Nat. Commun.* **2011**, *2*, No. 396.
- (7) Ramakrishna Matte, H. S. S.; Gomathi, A.; Manna, A. K.; Late, D. J.; Datta, R.; Pati, S. K.; Rao, C. N. R. MoS<sub>2</sub> and WS<sub>2</sub> Analogues of Graphene. *Angew. Chem., Int. Ed.* **2010**, *49*, 4059–4062.
- (8) Toh, R. J.; Sofer, Z.; Luxa, J.; Sedmidubský, D.; Pumera, M. 3R phase of MoS<sub>2</sub> and WS<sub>2</sub> outperforms the corresponding 2H phase for hydrogen evolution. *Chem. Commun.* **2017**, *53*, 3054–3057.
- (9) DiMasi, E.; Foran, B.; Aronson, M. C.; Lee, S. Stability of charge-density waves under continuous variation of band filling in LaTe<sub>2-x</sub>Sb<sub>x</sub> (0 < x < 1). *Phys. Rev. B* **1996**, *54*, 13587–13596.
- (10) Lei, S.; Teicher, S. M. L.; Topp, A.; et al. Band Engineering of Dirac Semimetals Using Charge Density Waves. *Adv. Mater.* **2021**, *33*, No. 2101591.
- (11) Salters, T. H.; Orlandi, F.; Berry, T.; Khoury, J. F.; Whittaker, E.; Manuel, P.; Schoop, L. M. Charge density wave-templated spin cycloid in topological semimetal  $NdSb_xTe_{2-x-\delta}$ . *Phys. Rev. Mater.* **2023**, 7, No. 044203.
- (12) Monceau, P. Electronic crystals: an experimental overview. *Adv. Phys.* **2012**, *61*, 325–581.
- (13) Yin, Y.; Aslandukova, A.; Jena, N.; et al. Unraveling the Bonding Complexity of Polyhalogen Anions: High-Pressure Synthesis of Unpredicted Sodium Chlorides Na2Cl3 and Na4Cl5 and Bromide Na4Br5. *JACS Au* **2023**, 3, 1634–1641.
- (14) Yannello, V. J.; Lu, E.; Fredrickson, D. C. At the Limits of Isolobal Bonding:  $\Pi$ -Based Covalent Magnetism in  $Mn_2Hg_5$ . *Inorg. Chem.* **2020**, *59*, 12304–12313.
- (15) Legrand, E. The magnetic structure of Mn<sub>2</sub>Hg<sub>5</sub>. Phys. Status Solidi A 1973, 15, K37–K39.
- (16) Ohashi, M. The Magnetic and Thermal Properties of the Intermetallic Compound MnHg. J. Phys. Soc. Jpn. 1965, 20, 911–914.
- (17) Ran, S.; Eckberg, C.; Ding, Q.-P.; Furukawa, Y.; Metz, T.; Saha, S. R.; Liu, I.-L.; Zic, M.; Kim, H.; Paglione, J.; Butch, N. P. Nearly ferromagnetic spin-triplet superconductivity. *Science* **2019**, *365*, 684–687.
- (18) Yang, J.; Luo, J.; Yi, C.; Shi, Y.; Zhou, Y.; qing Zheng, G. Spintriplet superconductivity in K<sub>2</sub>Cr<sub>3</sub>As<sub>3</sub>. *Sci. Adv.* **2021**, *7*, No. eabl4432, DOI: 10.1126/sciadv.abl4432.
- (19) Pollak, C. J.; Skorupskii, G.; Gutierrez-Amigo, M.; Singha, R.; Stiles, J. W.; Kamm, F.; Pielnhofer, F.; Ong, N. P.; Errea, I.; Vergniory, M. G.; Schoop, L. M. Chemical Bonding Induces One-Dimensional Physics in Bulk Crystal BiIr<sub>4</sub>Se<sub>8</sub>. *J. Am. Chem. Soc.* **2024**, *146*, 6784–6795.
- (20) Papoian, G. A.; Hoffmann, R. Hypervalent Bonding in One, Two, and Three Dimensions: Extending the Zintl–Klemm Concept to Nonclassical Electron-Rich Networks. *Angew. Chem., Int. Ed.* **2000**, 39, 2408–2448.
- (21) Arora, R.; Waghmare, U.; Rao, C. N. R. Metavalent Bonding in 2D Chalcogenides: Structural Origin and Chemical Mechanisms. *Angew. Chem., Int. Ed.* **2024**, *63*, No. e202313852.
- (22) Eschen, M.; Jeitschko, W. Au<sub>2</sub>PbP<sub>2</sub>, Au<sub>2</sub>TlP<sub>2</sub>, and Au<sub>2</sub>HgP<sub>2</sub>: Ternary Gold Polyphosphides with Lead, Thallium, and Mercury in the Oxidation State Zero. *J. Solid State Chem.* **2002**, *165*, 238–246.
- (23) Johrendt, D.; Mewis, A. BaPdP, Ba<sub>2</sub>PdP<sub>3</sub> und BaPd<sub>2</sub>P<sub>4</sub>-Zintl-Verbindungen oder intermetallische Phasen? *J. Alloys Compd.* **1994**, 205, 183–189.
- (24) Dünner, J.; Mewis, A. BaCu<sub>2</sub>P<sub>4</sub>-ein neues ternäres polyphosphid. *J. Less-Common Met.* **1990**, *167*, 127–134.
- (25) Keimes, V.; Johrendt, D.; Mewis, A. BaNi<sub>2</sub>P<sub>4</sub>: Dimorphie durch Peierls-Verzerrung? *Z. Anorg. Allg. Chem.* **1995**, *621*, 925–930.

- (26) Dolyniuk, J.-A.; Wang, J.; Lee, K.; Kovnir, K. Twisted Kelvin Cells and Truncated Octahedral Cages in the Crystal Structures of Unconventional Clathrates,  $AM_2P_4$  (A = Sr, Ba; M = Cu, Ni). *Chem. Mater.* **2015**, 27, 4476–4484.
- (27) Fulmer, J.; Lebedev, O. I.; Roddatis, V. V.; Kaseman, D. C.; Sen, S.; Dolyniuk, J.-A.; Lee, K.; Olenev, A. V.; Kovnir, K. Clathrate Ba<sub>8</sub>Au<sub>16</sub>P<sub>30</sub>: The "Gold Standard" for Lattice Thermal Conductivity. *J. Am. Chem. Soc.* **2013**, *135*, 12313–12323.
- (28) Dünner, J.; Mewis, A.  $Ba_8Cu_{16}P_{30}$  eine neue ternäre Variante des Clathrat I-Strukturtyps. Z. Anorg. Allg. Chem. **1995**, 621, 191–196
- (29) Dolyniuk, J.-A.; Zaikina, J. V.; Kaseman, D. C.; Sen, S.; Kovnir, K. Breaking the Tetra-Coordinated Framework Rule: New Clathrate  $Ba_8M_{24}P_{28+\delta}$  (M = Cu/Zn). *Angew. Chem., Int. Ed.* **2017**, *56*, 2418–2422.
- (30) Dolyniuk, J.; Whitfield, P. S.; Lee, K.; Lebedev, O. I.; Kovnir, K. Controlling superstructural ordering in the clathrate-I  $Ba_8M_{16}P_{30}$  (M = Cu, Zn) through the formation of metal-metal bonds. *Chem. Sci.* **2017**, *8*, 3650–3659.
- (31) Wang, J.; Dolyniuk, J.-A.; Kovnir, K. Unconventional Clathrates with Transition Metal-Phosphorus Frameworks. *Acc. Chem. Res.* **2018**, *51*, 31–39.
- (32) Wen, X.-D.; Cahill, T. J.; Hoffmann, R. Element Lines: Bonding in the Ternary Gold Polyphosphides, Au<sub>2</sub>MP<sub>2</sub> with M = Pb, Tl, or Hg. *J. Am. Chem. Soc.* **2009**, *131*, 2199–2207.
- (33) Janssen, E. M. W.; Wiegers, G. Crystal growth and the crystal structures of two modifications of gold monobromide, I-AuBr and P-AuBr. J. Less-Common Met. 1978, 57, P47–P57.
- (34) Monteseguro, V.; Errandonea, D.; Achary, S. N.; Sans, J. A.; Manjón, F. J.; Gallego-Parra, S.; Popescu, C. Structural Characterization of Aurophilic Gold(I) Iodide under High Pressure. *Inorg. Chem.* **2019**, *58*, 10665–10670.
- (35) Strähle, J.; Lörcher, K.-P. Notizen: Die Kristalldaten der Goldhalogenide AuBr<sub>3</sub> und AuCl/The Lattice Parameters of the Gold Halogenides AuBr<sub>3</sub> and AuCl. *Z. Naturforsch.* **1974**, *29*, 266–267.
- (36) Khoury, J. F.; Han, B.; Jovanovic, M.; Singha, R.; Song, X.; Queiroz, R.; Ong, N.-P.; Schoop, L. M. A Class of Magnetic Topological Material Candidates with Hypervalent Bi Chains. *J. Am. Chem. Soc.* **2022**, *144*, 9785–9796.
- (37) Khoury, J. F.; Song, X.; Schoop, L. M.  $Ln_3MBi_5$  (Ln=Pr, Nd, Sm; M=Zr, Hf): Intermetallics with Hypervalent Bismuth Chains. Z. Anorg. Allg. Chem. **2022**, 648, No. e202200123.
- (38) Tkachuk, A. V.; Crerar, S. J.; Wu, X.; Muirhead, C. P. T.; Deakin, L.; Mar, A. Structures and Physical Properties of Ternary Antimonides  $RE_3MSb_5$  (M = Zr, Hf),  $U_3MSb_5$  (M = Zr, Hf, Nb), and YbCrSb<sub>3</sub>. MRS Online Proc. Libr. 2004, 848, 141–148.
- (39) APEX Inc. APEX2, 2012 (accessed Aug 07, 2023).
- (40) Petříček, V.; Palatinus, L.; Plášil, J.; Dušek, M. Jana2020 a new version of the crystallographic computing system Jana. Z. Kristallogr.—Cryst. Mater. 2023, 238, 271–282.
- (41) Gonze, X.; Amadon, B.; Anglade, P. M.; et al. ABINIT: First-principles Approach to Material and Nanosystem Properties. *Comput. Phys. Commun.* **2009**, *180*, 2582–2615.
- (42) Gonze, X.; Rignanese, G.-m.; Verstraete, M.; Beuken, J.-m.; Pouillon, Y.; Caracas, R.; Raty, J.-y.; Olevano, V.; Bruneval, F.; Reining, L.; Godby, R.; Onida, G.; Hamann, D. R.; Allan, D. C. A Brief Introduction to the ABINIT Software Package. *Z. Kristallogr.—Cryst. Mater.* **2005**, 220, 558–562.
- (43) Hartwigsen, C.; Goedecker, S.; Hutter, J. Relativistic Separable Dual-space Gaussian Pseudopotentials from H to Rn. *Phys. Rev. B* **1998**, *58*, 3641–3662.
- (44) Kresse, G.; Hafner, J. Ab initio molecular dynamics for liquid metals. *Phys. Rev. B* **1993**, *47*, 558–561.
- (45) Kresse, G.; Furthmüller, J. Efficient iterative schemes for ab initio total-energy calculations using a plane-wave basis set. *Phys. Rev.* B **1996**, *54*, 11169–11186.
- (46) Kresse, G.; Furthmüller, J. Efficiency of ab-initio total energy calculations for metals and semiconductors using a plane-wave basis set. *Comput. Mater. Sci.* **1996**, *6*, 15–50.

- (47) Blöchl, P. E. Projector augmented-wave method. *Phys. Rev. B* **1994**, *50*, No. 17953.
- (48) Kresse, G.; Joubert, D. From ultrasoft pseudopotentials to the projector augmented-wave method. *Phys. Rev. B* **1999**, *59*, 1758–1775
- (49) Eckhardt, C.; Hummer, K.; Kresse, G. Indirect-to-direct gap transition in strained and unstrained  $Sn_xGe_{1-x}$  alloys. *Phys. Rev. B* **2014**, 89, No. 165201.
- (50) Ganose, A. M.; Jackson, A. J.; Scanlon, D. O. sumo: Commandline tools for plotting and analysis of periodic ab initio calculations. *J. Open Source Software* **2018**, *3*, No. 717.
- (51) Pan, F.; Guggolz, L.; Weigend, F.; Dehnen, S. Atom Exchange Versus Reconstruction:  $(Ge_xAs_{4-x})^{x-}$  (x = 2, 3) as Building Blocks for the Supertetrahedral Zintl Cluster  $[Au_6(Ge_3As)(Ge_2As_2)_3]^{3-}$ . Angew. Chem., Int. Ed. **2020**, 59, 16638–16643.
- (52) Adams, R. D.; Elpitiya, G. The Addition of Gold and Tin to Bismuth-Triiridium Carbonyl Complexes. *Inorg. Chem.* **2015**, *54*, 8042–8048.
- (53) Ke, I.-S.; Gabbaï, F. P. σ-Donor/Acceptor-Confused Ligands: The Case of a Chlorostibine. *Inorg. Chem.* **2013**, 52, 7145–7151.
- (54) Jansen, M. The chemistry of gold as an anion. *Chem. Soc. Rev.* **2008**, *37*, 1826–1835.
- (55) Tang, Z.; Litvinchuk, A. P.; Lee, H.-G.; Guloy, A. M. Crystal Structure and Vibrational Spectra of a New Viologen Gold(I) Iodide. *Inorg. Chem.* **1998**, *37*, 4752–4753.
- (56) Schmidbaur, H.; Schier, A. Aurophilic interactions as a subject of current research: an up-date. *Chem. Soc. Rev.* **2012**, *41*, 370–412.
- (57) Kim, S.-J.; Miller, G. J.; Corbett, J. D. Zigzag Chains of Alternating Atoms in A2AuBi (A = Na, K) and K2AuSb. Synthesis, Structure, and Bonding. *Z. Anorg. Allg. Chem.* **2010**, *636*, *67*–73.
- (58) Lee, S. J.; Won, J.; Wang, L.-L.; Jing, D.; Harmer, C. P.; Mark, J.; Akopov, G.; Kovnir, K. New Noncentrosymmetric Tetrel Pnictides Composed of Square-Planar Gold(I) with Peculiar Bonding. *Chem.—Eur. J.* **2021**, 27, 7383–7390.
- (59) Fulmer, J.; Kaseman, D. C.; Dolyniuk, J.-A.; Lee, K.; Sen, S.; Kovnir, K. BaAu2P4: Layered Zintl Polyphosphide with Infinite  $_{\infty}^{1}(P^{-})$  Chains. *Inorg. Chem.* **2013**, *52*, 7061–7067.
- (60) Osman, H. H.; Salvadó, M. A.; Pertierra, P.; Engelkemier, J.; Fredrickson, D. C.; Recio, J. M. Chemical Pressure Maps of Molecules and Materials: Merging the Visual and Physical in Bonding Analysis. *J. Chem. Theory Comput.* **2018**, *14*, 104–114.
- (61) Kamp, K. R.; Fredrickson, D. C. A Tour of Soft Atomic Motions: Chemical Pressure Quadrupoles Across Transition Metal—Main Group 1:2 Structure Types. *Chem. Mater.* **2022**, *34*, 10011–10024.
- (62) Schoop, L. M.; Pielnhofer, F.; Lotsch, B. V. Chemical Principles of Topological Semimetals. *Chem. Mater.* **2018**, *30*, 3155–3176.
- (63) Gibson, Q. D.; Schoop, L. M.; Muechler, L.; Xie, L. S.; Hirschberger, M.; Ong, N. P.; Car, R.; Cava, R. J. Three-dimensional Dirac semimetals: Design principles and predictions of new materials. *Phys. Rev. B* **2015**, *91*, No. 205128.